Improved mechanical properties of a Ti-48Al alloy processed by mechanical alloying and spark plasma sintering

V. Sharma [a], X. Tan [a], P.S. Sankara Rama Krishnan [a], Sravya Tekumalla [b], M. Duchamp [a], Xuesong Xu [c], Hongsheng Ding [c], V. Chaudhary [d,*], R.V. Ramanujan [a,*]

[a] *School of Materials Science and Engineering, Nanyang Technological University, Singapore 639798, Singapore*
[b] *School of Mechanical and Aerospace Engineering, Nanyang Technological University, Singapore 639798, Singapore*
[c] *School of Materials Science and Engineering, Harbin Institute of Technology, Harbin 150001, China*
[d] *Industrial and Materials Science, Chalmers University of Technology, SE-41296 Gothenburg, Sweden*

Abstract:

Bulk Ti-48Al alloy samples were prepared by the high energy ball milling (HBM) of elemental powders, followed by spark plasma sintering (SPS) of the HBM processed powders. The microstructure, phase evolution and mechanical properties of the bulk alloy were studied. The resulting TiAl + Ti_3Al two phase alloy possessed an equiaxed fine grain structure, unlike the usual lamellar structure produced by arc melting. The process parameters of HBM and SPS, e.g., milling speed, milling time and sintering temperature were used to tune the phase fraction, microstructure, and grain size. A very high nanohardness of up to ~12 GPa was obtained, ~2.4 times higher than the corresponding value of the as-cast counterpart. The combined influence of powder size reduction during HBM, high Ti_3Al phase fraction and microstructural development during SPS resulted in higher hardness, wear resistance and yield pressure. Thus, a HBM+SPS processing approach is a promising processing route for the manufacture of high hardness bulk TiAl alloys.

Keywords: Ti-Al alloys Mechanical alloying Spark plasma sintering Microstructures Structural properties

1. Introduction

Intermetallic TiAl based alloys have attracted considerable attention as lightweight structural materials which can potentially replace nickel-based superalloys in certain aerospace, energy, and automobile applications [1–5]. These alloys show an excellent combination of properties, such as low density (3.8–4.1 gcm^{-3}) [6], high strength to weight ratio, good creep properties up to 900 °C, high melting point (1460 °C) and excellent resistance to corrosion and oxidation [7,8]. Aerospace components manufactured using such alloys include compressors, nozzles, high speed components, transition duct beams and combustors [3,9]. The microstructure of TiAl alloys produced by the casting route is a lamellar [10] structure, comprising of parallel plates of the chemically ordered γ ($L1_0$) and α_2 ($D0_{19}$) phases, and a small fraction of equiaxed γ grains [11–13].

A major challenge in the processing of cast TiAl based alloys is their low workability, which severely hampers the production of complex geometries [12]. Methods to improve the workability, oxidation resistance and mechanical properties by adding alloying elements, e.g., Cr, Mn, Nb, Ta, W, B to the binary Ti-48Al composition have been investigated [14–16]. The microstructure-property relationships have also been studied for such alloy compositions. The various length scales of the lamellar sizes and colonies critically influences the mechanical properties. The strength is usually governed by a Hall-Petch type relationship [17]. Alloys with a fully lamellar structure exhibit superior fracture toughness [5] and creep resistance [18].

The traditional casting process for TiAl alloys, although successfully deployed in critical industrial applications, can lead to structural inhomogeneities with compromised properties. Hence, the alternative powder metallurgy (PM)-based route has garnered significant attention. The PM process yields a fine-grained microstructure, which results in improved strength and ductility. Despite this advantage, full densification by traditional PM based techniques can only be achieved after long process cycles [19]. On the other hand, spark plasma sintering (SPS) is a fast technique in which powders are sintered to high density by the simultaneous application of pressure and a swift temperature rise induced by a DC electrical current. Due to both these factors, this process is highly energy efficient and grain growth can be minimized [9].

Table 1
Sample name and processing conditions.

Sample name	HBM speed (RPM)	HBM time	Milling intensity [31]	SPS temperature (°C)	SPS time (min)
P1	N/A	N/A	N/A	N/A	N/A
P2	300	4 h	6	N/A	N/A
P3	400	5 h	8	N/A	N/A
S1	N/A	N/A	N/A	1000	5
S2	300	4 h	6	1000	5
S3	400	5 h	8	1000	5

Recently, additive manufacturing routes such as selective laser melting [20] and electron beam melting [21] have also been trialled for TiAl based alloys.

Previous studies on the use of SPS as a processing route for this family of alloys used pre-alloyed gas atomized TiAl powders as the starting material [22–29]. However, gas atomization is a very expensive process. Hence, an alternate cheaper approach, such as mechanical alloying of elemental Ti and Al powders using high energy ball milling (HBM), is very attractive. The milling speed and milling time of HBM can be varied to produce a range of particle sizes. Deformation and alloying of powder particles and attrition of the powders by the milling media during high-speed rotation results in homogeneously mixed powders. The rapid heating and short duration of the subsequent SPS process of these HBM powders can produce bulk TiAl based alloys with unique microstructures and improved mechanical properties.

In this work, we report the processing, characterization, and property evaluation of Ti48Al alloys prepared by a combination of HBM and SPS techniques. A significant change in the microstructure as well as hardness and strength were observed with a change of the HBM process parameters. This HBM+SPS process resulted in a nano hardness of up to 12 GPa, which is ~ 2.4 times of the value obtained from conventional as cast material. The higher volume fraction of the α_2Ti_3Al phase obtained at higher HBM speed and duration can account for the improved room temperature mechanical properties. These results suggest that HBM+SPS can be an alternative promising processing route for TiAl based alloys.

2. Experimental methods

The mass of Ti (99%, Alfa Aesar) and Al (99.5%, Alfa Aesar) powders were chosen corresponding to the nominal Ti48Al composition. The powders were milled in a Fritsch Pulverisette-7 planetary ball mill. The ball to powder ratio was 10:1, the vials, and the balls (10 mm) were made of zirconium oxide. A few drops of ethanol were added as a process control agent to prevent cold welding. Table 1 presents the nomenclature used and the experimental conditions of the samples. Two ball milling speeds were selected. Powder P1 was a mixture of elemental Ti and Al powders, which was not ball milled. This sample was the reference to determine the effect of HBM. Powder P2 was milled at 300 rpm for 4 h, powder P3 was milled at 400 rpm for 5 h. Assessment of the milling intensity [30] was performed based on the formulae reported by Suryanarayana for Fritsch Pulverisette-7 planetary ball mills [31].

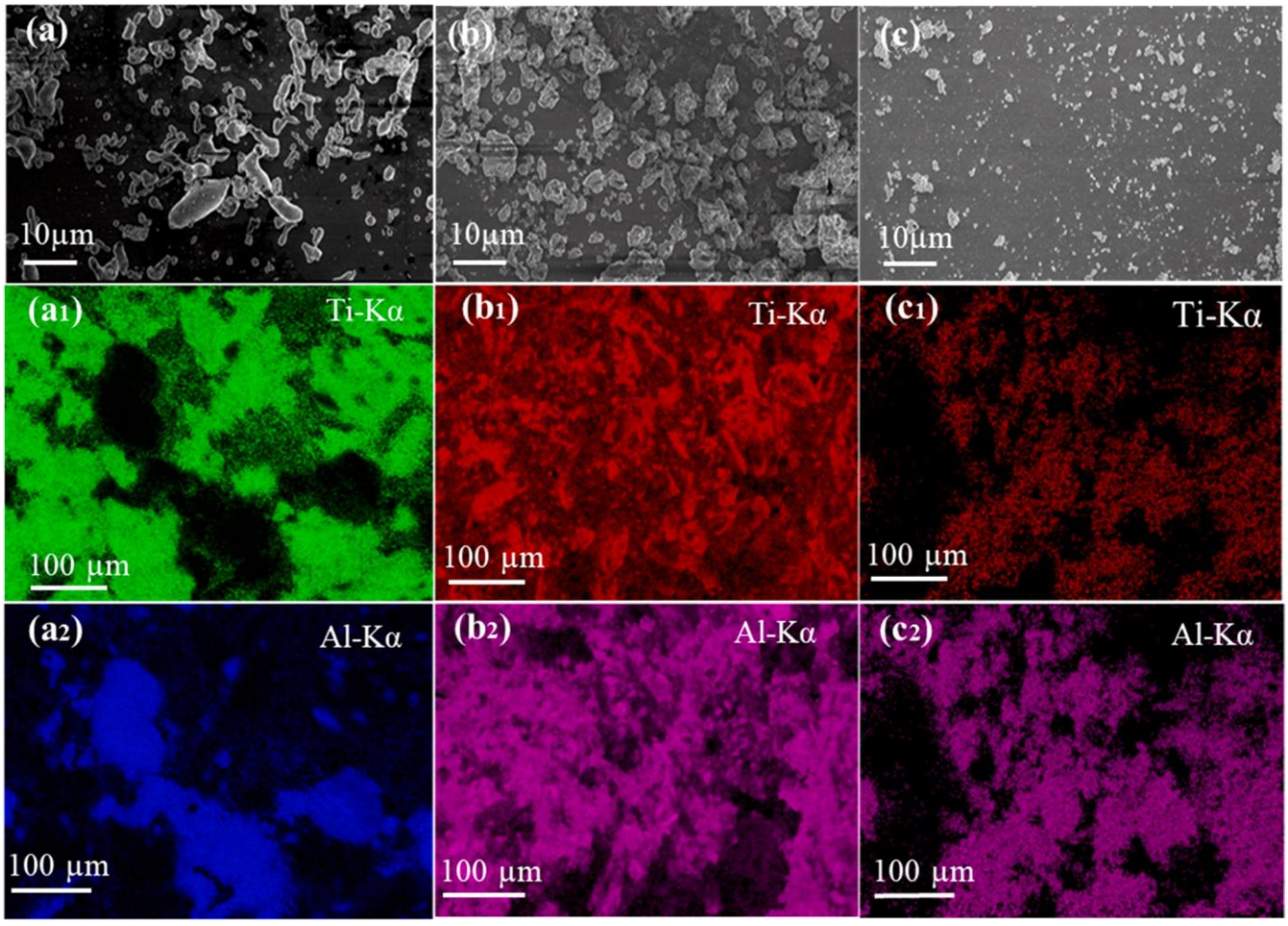

Fig. 1. SEM secondary electron images of sample (a) P1, (b) P2, and (c) P3, and SEM-EDS images for (a_1, b_1, c_1) Ti and (a_2, b_2 c_2) Al elemental mapping for P1, P2 and P3 samples, respectively.

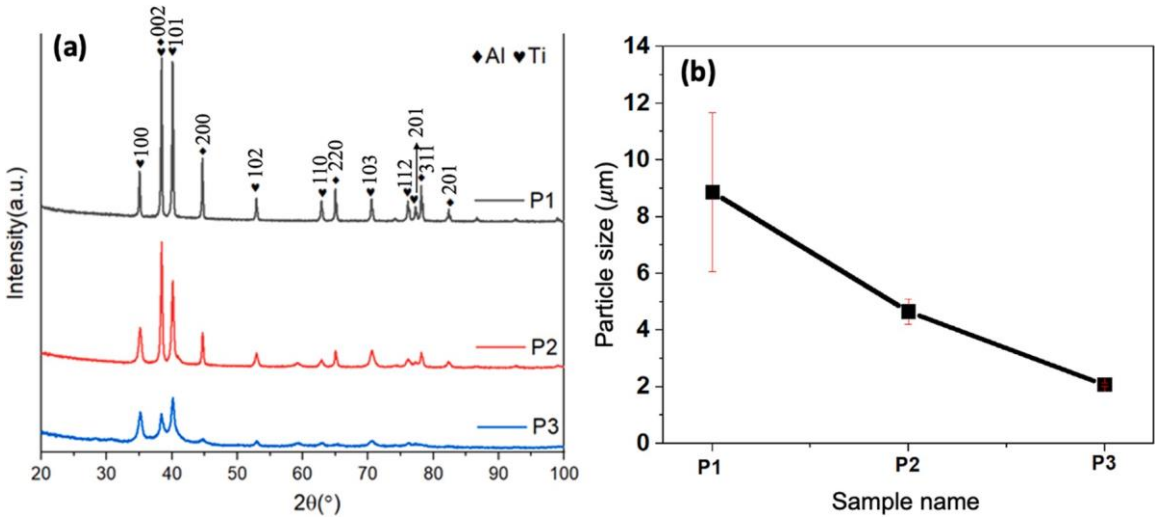

Fig. 2. (a) XRD patterns of samples P1, P2 and P3, and (b) average particle size for samples P1, P2, and P3. If the position of Al and Ti diffraction peaks at the same 2θ values, they are indexed only for Ti.

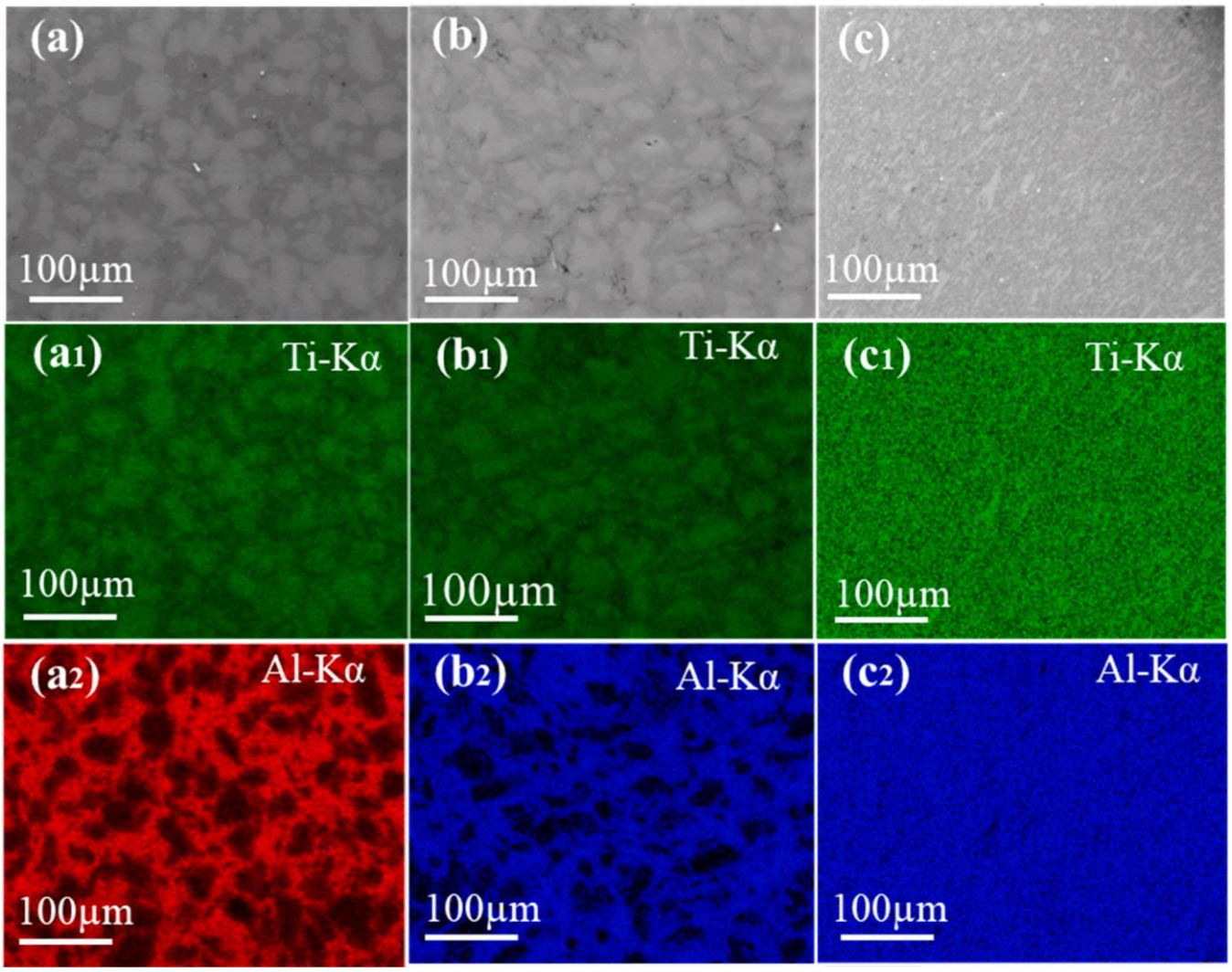

Fig. 3. SEM-BSE and corresponding SEM-EDS images of SPS samples S1, S2, S3, respectively.

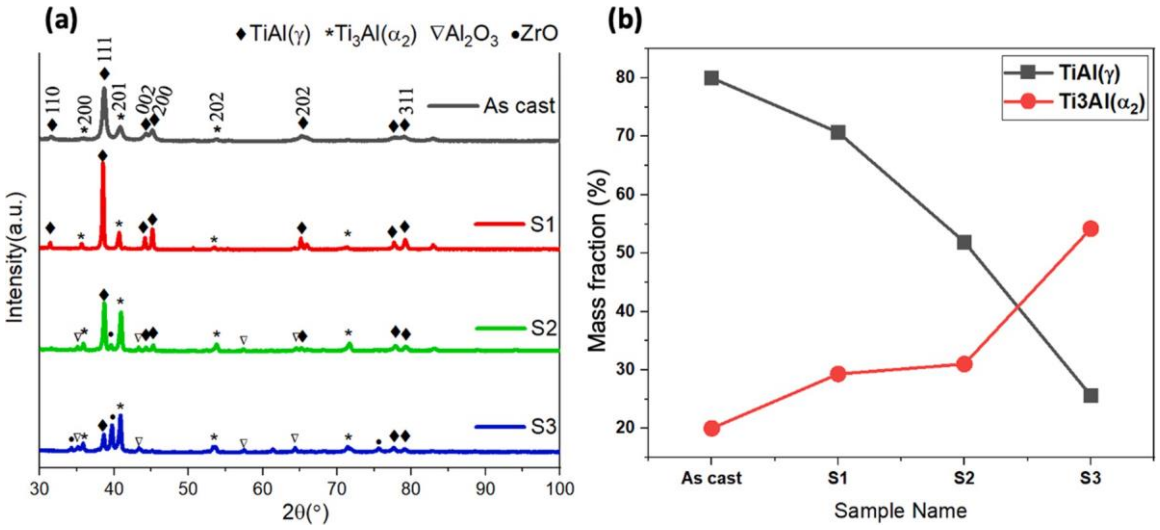

Fig. 4. (a) XRD patterns of the SPS (S1, S2, S3) and as cast samples, (b) mass fraction of α2 and γ phases obtained from Rietveld refinement of the XRD data shown in (a).

P1, P2 and P3 were separately sintered in a Spark Plasma Sintering equipment (Fuji Electronic Industrial, SPS-211LX) at a vacuum level less than 8 Pa. 5 g of the powder was filled in a graphite cylindrical die with a diameter of 10 mm and height of 20 mm. The powders P1, P2 and P3 were subjected to SPS, the corresponding bulk solid samples are designated as S1, S2 and S3, respectively.

SPS was performed at 1000 °C for 5 min at an applied pressure of 50 MPa and a heating rate of 60 °C/min. After sintering, the samples were cooled inside the SPS chamber. For a broader understanding of the microstructural evolution, additional experiments were carried out for the P3 sample, which showed higher nano-hardness after SPS. The P3 powder was subjected to SPS for 5 min at a range of temperatures from 900° to 1200°C. A Ti-48Al as-cast sample was also prepared by arc melting to compare the cast microstructure and mechanical properties with those of the SPS samples. Samples S1 to S3 and the as-cast sample were cut and prepared by standard metallographic techniques.

X-ray diffraction was performed using a Bruker D-8 (Advanced) XRD in Bragg-Brentano (θ-2θ) configuration (CuKα radiation, λ = 0.154 nm). Rietveld refinement of the XRD patterns was performed using the "TOPAS" software. A JEOL-7800 field emission scanning electron microscope (FESEM), equipped with a Symmetry S2 electron back scattered diffraction (EBSD) detector (Oxford Instruments, UK) was used to assess the microstructure of the samples. We employed EBSD using a step size of 0.3 μm, and the selected phases are TiAl (γ, Tetragonal, P4/mmm) and Ti3Al (α2, Hexagonal, P63/mmc).

The nanoindentation tests were performed using a Nanoindenter G200 (KLA Tencor, Milpitas, CA, USA) instrument equipped with a Berkovich tip in load-controlled mode, at a maximum load of 100 mN and a loading rate of 0.5 mN/s. Force and displacement were continuously measured during the indentation. 30 indentation measurements were performed for each sample. The Oliver-Pharr method was employed to calculate the elastic modulus and hardness.

3. Results and discussion

3.1. Microstructure and phase analysis of powders

The surface morphology of the powder samples in the as milled condition is shown in Fig. 1 (a1-a3). The scanning electron microscope (SEM) images of the samples revealed that the morphology varies with milling intensity. The scanning electron microscope-energy dispersive spectroscopy (SEM-EDS) maps of Ti-Kα and Al-Kα of the samples P1, P2 and P3 are shown in Fig. 1(b1-b3, c1-c3), respectively.

In the case of the P1 sample spatially distinct - anti correlated - Ti-Kα and Al-Kα signals are observed (Fig. 1 b1-c1), as expected. The P2 sample, with the lower milling intensity, shows a predominant contrast for Al-Kα (Fig. 1 (b2-c2)), with little spatial correlation with the Ti-Kα signal, indicating a non-uniform coating of Al around the Ti particles. The P3 sample with the higher milling intensity sample shows a spatial correlation between the Ti-Kα and Al-Kα signals (Fig. 1 (b3-c3)), indicating more uniform mixing of the elemental Ti and Al powders.

Fig. 2(a) shows the XRD patterns of the P1, P2 and P3 powders. In sample P2, the peak intensity for fcc Al (2θ at 45°) shows a significant reduction compared to that of sample P1. In sample P3, the intensity of diffraction peaks is reduced further, indicating the dissolution of Al in Ti [32]. The mixed elemental powder (P1) shows a particle size ranging from 8 to 12 μm, the particle size decreases to 2–4 μm with an increase in ball milling time and duration (P2 and P3), Fig. 2(b) clearly shows this trend.

3.2. Microstructure and phase analysis of SPS samples

The SEM-BSE images and SEM-EDS mapping of S1, S2 and S3 samples are shown in Fig. 3(a-c), respectively. The difference in contrast distribution for the Ti-Kα and Al-Kα EDX signals in S2 and S3 samples indicates the effect of the more homogeneous morphology in sample P3 compared to sample P2.

The XRD data and Rietveld refinement of the XRD data of the samples after SPS are shown in Fig. 4(a). In all the SPS samples, both the γ TiAl phase and the α_2 Ti_3Al phase were present. The mass fraction of the α_2Ti_3Al phase increased significantly for the sample S3 prepared from the higher milling intensity powder (P3) at the expense of the γ TiAl phase content (Fig. 4(b)). *This important observation confirmed that the relative mass fraction of the phases can be tuned by changing the milling intensity of HBM. This is a key advantage of the HBM+SPS process compared to the casting processing route.* Combining the XRD and SEM-EDS results, one can observe that when ball milling speed and duration is increased, the formation of α_2Ti_3Al is significantly facilitated, and its mass fraction is much higher than the equilibrium mass fraction of the α_2Ti_3Al phase for Ti-48Al.

Fig. 5 shows the EBSD band contrast and orientation images of the samples. Band contrast (BC) is an electron backscatter scattered patterns (EBSP) quality factor, obtained from the Hough transform, that describes the average intensity of the Kikuchi bands with respect to the overall intensity within the EBSP. The EBSP at grain boundaries tend to show poor band contrast, hence they appear dark in a map. The as cast

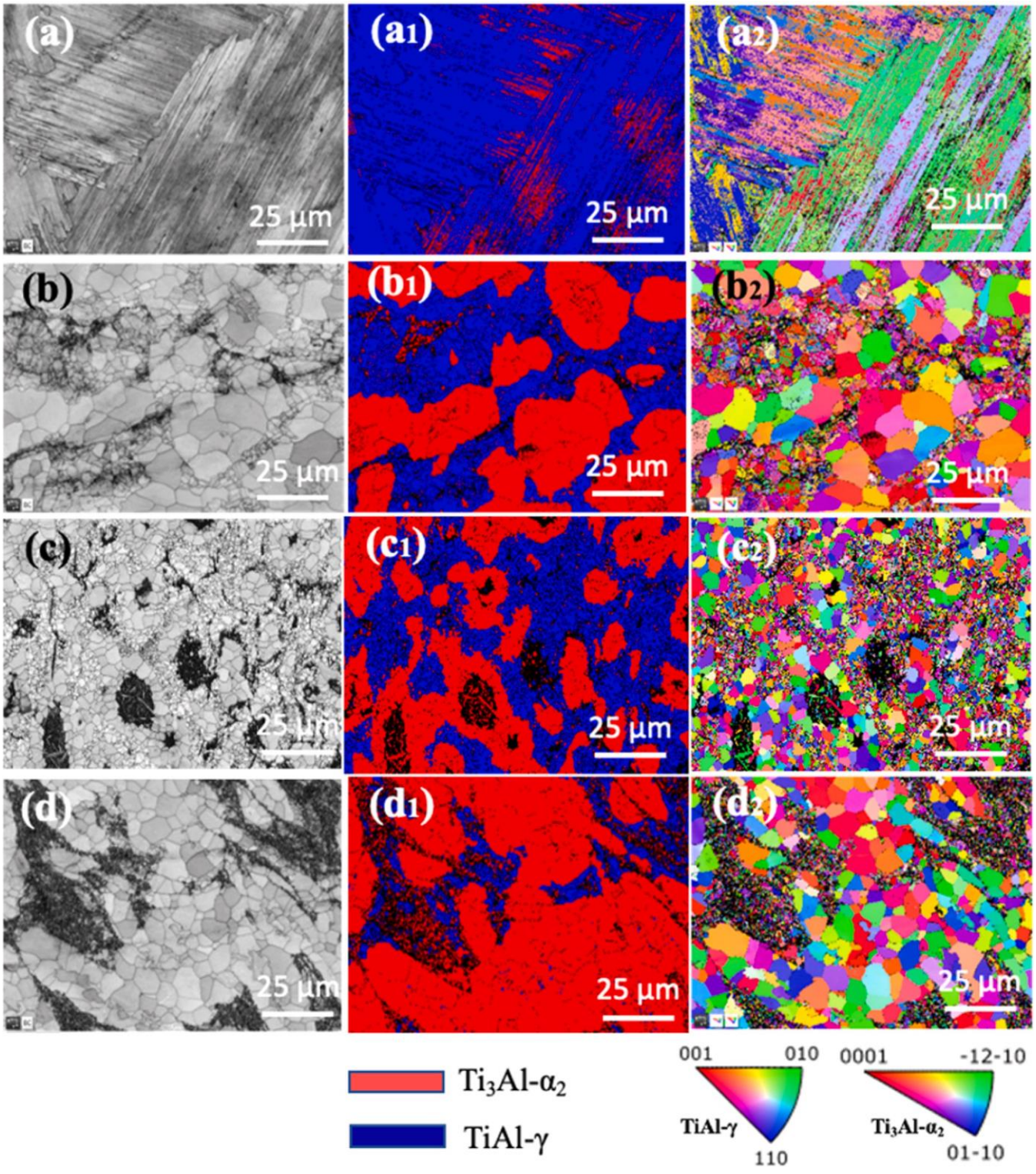

Fig. 5. EBSD band contrast and orientation mapping of as cast (a-a2), S1 (b-b2), S2 (c-c2) and S3 (d-d2) samples.

sample (Fig. 5(a-a2) shows the characteristic lamellar structure. On the other hand, the S1 sample shows a non-lamellar polycrystalline matrix with a roughly equal phase fraction of γTiAl and α_2Ti_3Al phases. The S2 sample shows a reduced distribution of γTiAl and equiaxed α_2Ti_3Al matrix. The S3 sample shows equiaxed grains of a α_2Ti_3Al matrix and a random distribution of the γTiAl phase. The γTiAl phase has a much smaller average size as compared to the α_2Ti_3Al phase.

The average grain size of both the Ti_3Al and the TiAl phases, for samples S1, S2 and S3, based on the EBSD analysis is shown in Fig. 6(a-c) respectively. The variation in the grain sizes can be clearly seen. The non-lamellar microstructure formation in the HBM+SPS sample can be related to the alloy formation temperature and subsequent phase evolution (Section 3.4).

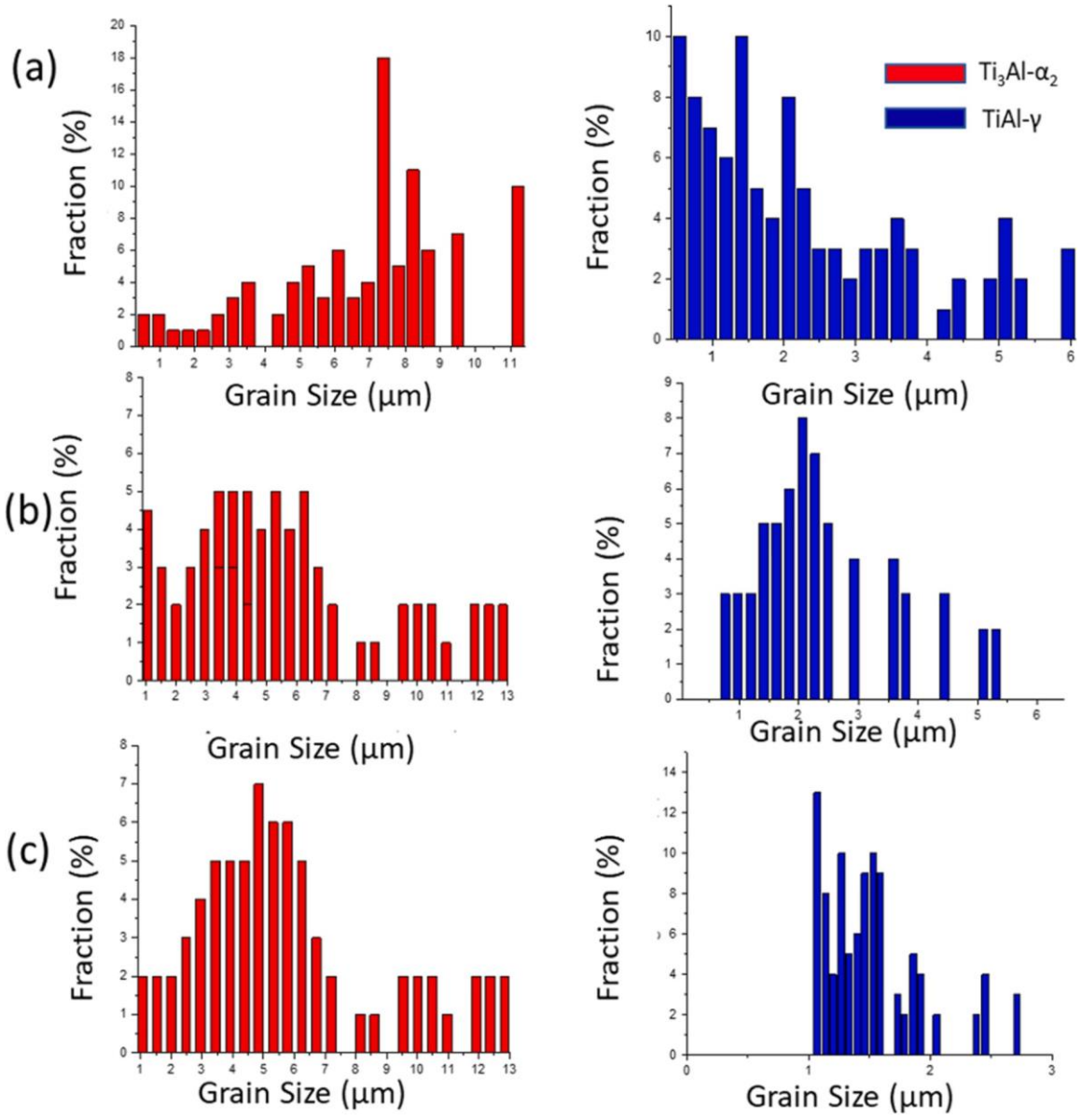

Fig. 6. Average grain size measurement based of EBSD analysis for sample (a) S1, (b) S2 and (c) S3.

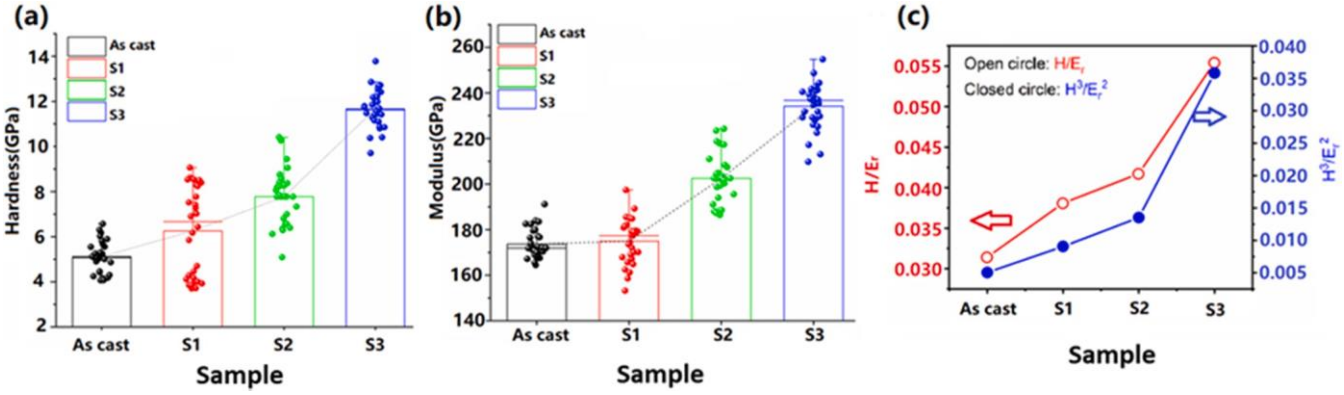

Fig. 7. (a) Nanohardness, (b) Elastic modulus, and (c) wear resistance, yield pressure of as cast and SPS samples.

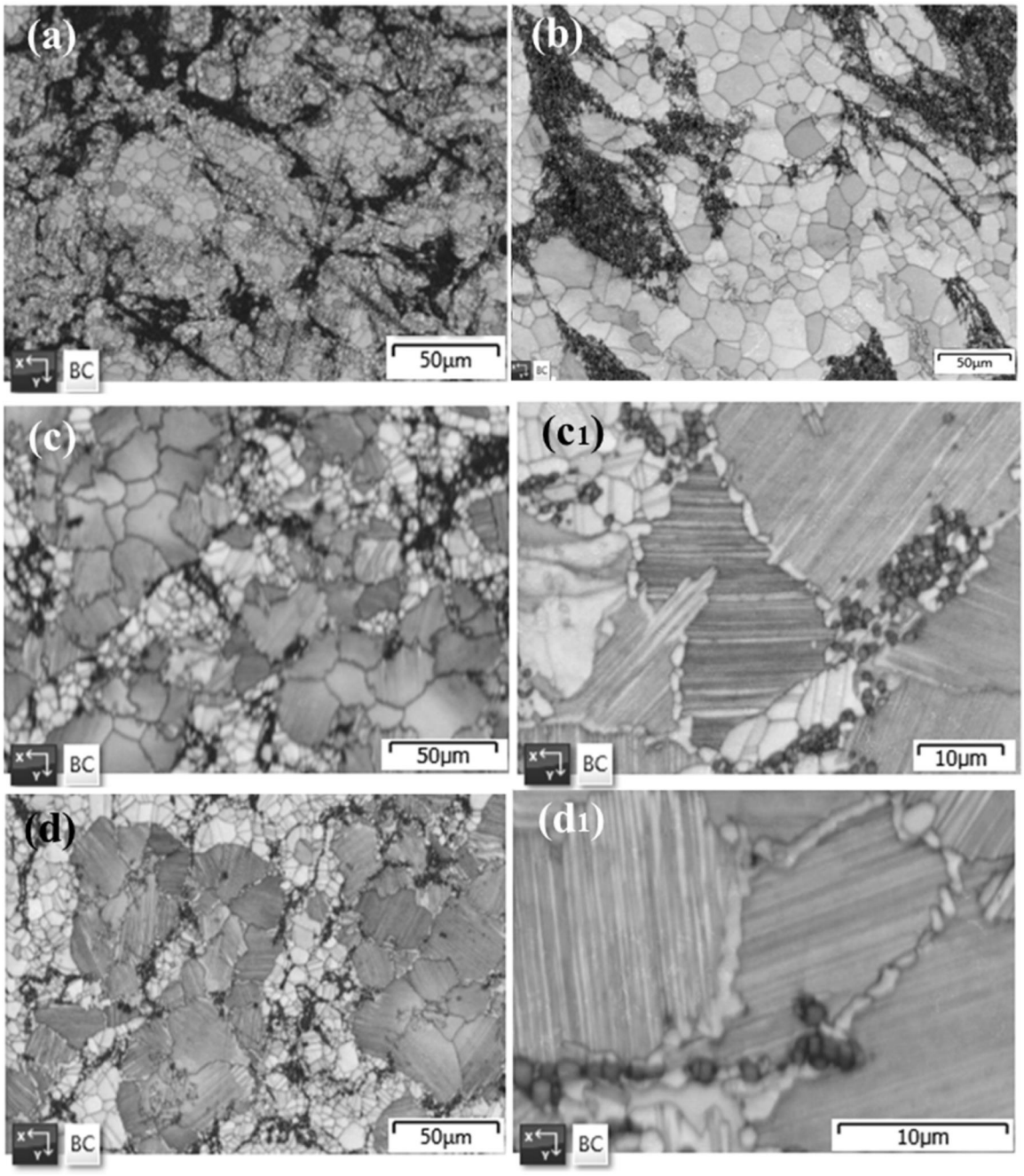

Fig. 8. Band contrast image obtained from EBSD for SPS samples sintered at (a) 900 °C, (b) 1000 °C, (c) 1100 °C, and (d) 1200 °C. The c_1 and d_1 images are magnified images of c and d.

Table 2
Phase fraction of SPS sample sintered at various temperatures.

SPS temperature (°C)	α_2-Ti_3Al phase fraction (%)	γ-TiAl phase fraction (%)
900	29	71
1000	60	40
1100	28	72
1200	68	32

3.3. Mechanical properties

Fig. 7(a and b) shows the hardness and modulus measured from nanoindentation. The HBM+SPS (S2 and S3) samples show significantly higher elastic modulus and hardness compared with the as cast and the S1 sample. This high value of hardness can be related to the microstructure evolution during the HBM+ SPS process. The nano hardness of S3 reached a high value of 12 GPa, which is significantly larger than the nanohardness values of both the α_2Ti_3Al (7.4–9.5 GPa) [33] and the γTiAl (4.2 – 6 GPa) individual phases.

The resistance to deform can be represented by the ratio of nanohardness to reduced modulus (H/Er) [34]. Another ratio related to wear is H^3/Er^2, the yield pressure or resistance to plastic deformation [34,35]. *Compared with commercial pure Ti and Ti-TiB composite materials, the Ti48Al alloy shows higher values of H/Er and H^3/Er^2, implying improved wear properties* [34]. For the SPS samples, larger values of H/Er and H^3/Er^2 are obtained with increasing ball milling speed and duration (Fig. 7(c)), suggesting that better wear resistance can be obtained from samples subjected to higher milling intensity followed by SPS. This

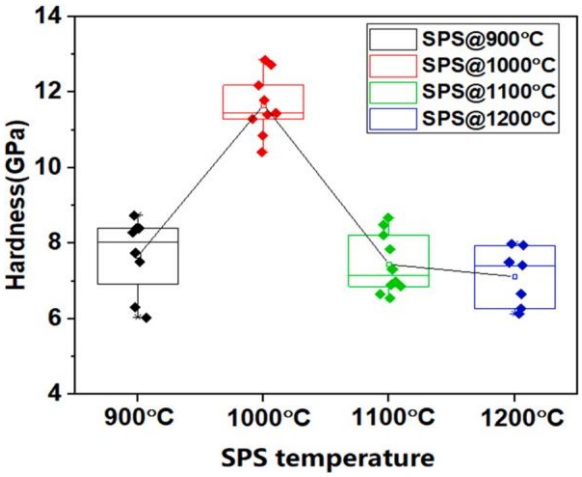

Fig. 9. Nanohardness of P3 powder after SPS at different temperatures from 900 °C to 1200 °C.

phenomenon may attribute to a marked increase in α_2 content and a rapid decrease in grain size, causing the change in hardness to be greater than that in elastic modulus. The S3 samples shows a H/Er ratio larger than the commercial Ti6Al4V alloy, and a H^3/Er^2 ratio larger than Ti31Fe9Sn and Ti39.3Nb13.3Zr10.7Ta alloy, suggesting superior wear resistance and yield pressure [36].

3.4. *Effect of SPS temperature on the microstructure*

Fig. 8(a-d) shows the band contrast image obtained from EBSD for SPS samples sintered for 5 min at 900, 1000, 1100, 1200 °C, respectively. The SPS samples sintered at 900 °C and 1000 °C showed fine equiaxed grains with no lamellar structure; higher sintering temperatures resulted in grain growth. On further increase of the SPS temperature to 1100 °C and 1200 °C formation of the lamellar structure was observed (Fig. 8(c1) and 8(d1)). Equiaxed grains in the size range of 1–3 μm were also formed along the lamellar colony boundaries.

According to the phase diagram, the eutectoid temperature (T_e) of Ti-48Al is ~1120 °C [37]. When SPS was performed at a temperature of 1000 °C, equiaxed grains of the α_2 and γ phases were observed in the sample. On the other hand, when the nominal SPS temperature increased to 1100 °C and 1200 °C, the local temperatures can be above T_α, i.e., in the α + γ region. The microstructure at that temperature consists of α grains and γ grains. During cooling, the phase transformation of a lamellar (α_2 + γ) structure occurs in the α phase, resulting in a duplex microstructure, consisting of equiaxed grains and α_2/γ lamellar colonies. The phase fraction of SPS sample sintered at 900 °C, 1000 °C 1100 °C and 1200 °C, based on the XRD results, is given in Table 2.

Nanoindentation was also performed on the SPS samples which were sintered at different temperatures (Fig. 9). The highest nanohardness is

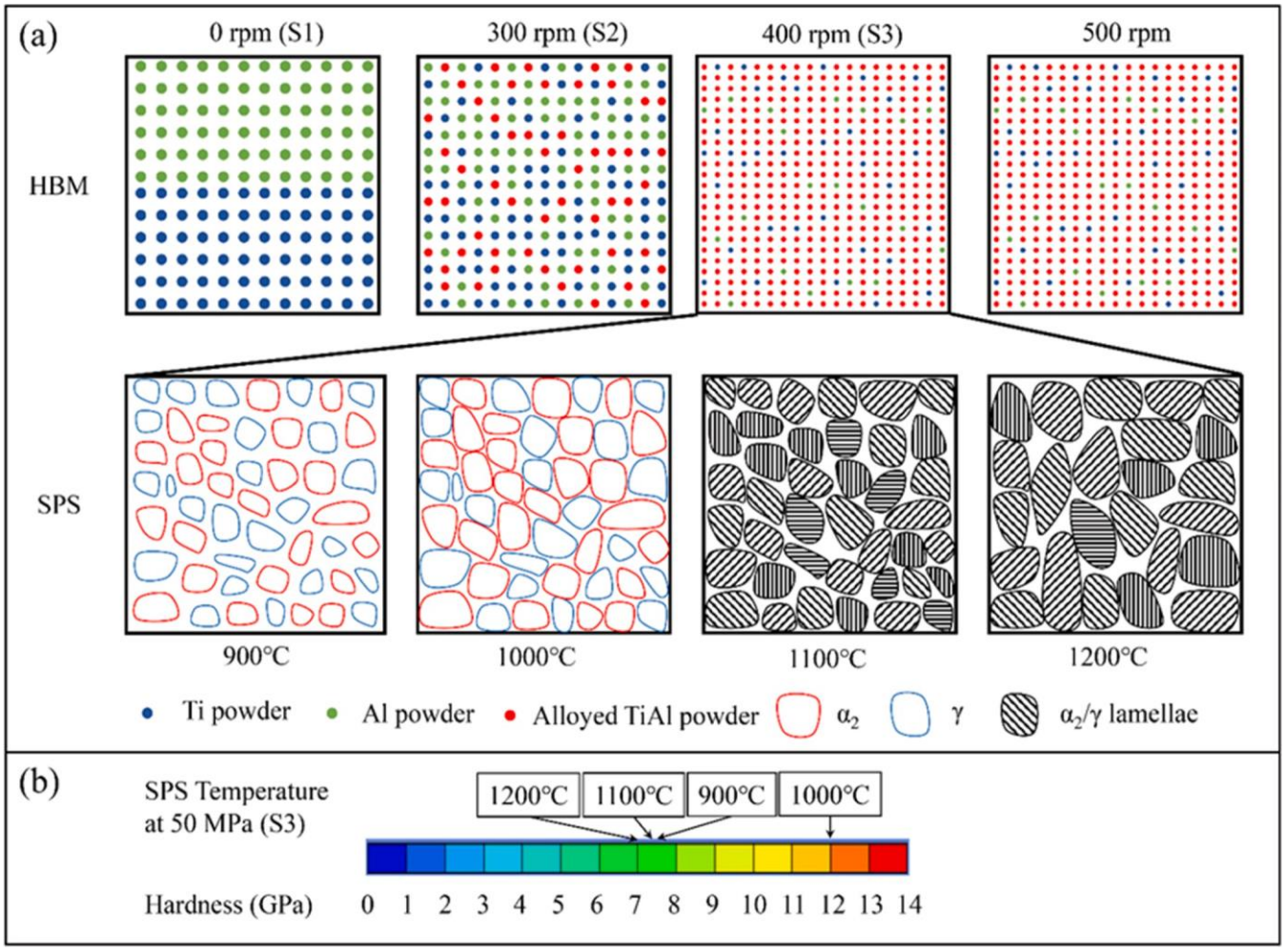

Fig. 10. (a) Schematic of the effect of HBM with various speeds and their influence on Ti48Al alloy microstructural evolution after SPS, (b) The hardness variation of SPS sample (S3) at different temperatures.

observed in the SPS sample sintered at 1000 °C. When the sintering temperature increased from 900° to 1000°C, the nanohardness increased from 7.5 to 12 GPa. This can be explained by the relatively low level of densification and lower interparticle bonding of the samples sintered at a SPS temperature of 900 °C [38]. When the sintering temperature was increased beyond 1000 °C, to 1100 °C and 1200 °C, the nanohardness decreased monotonically to 7 GPa. The increase of SPS temperature can change the grain size and lead to the formation of the lamellar structure, both these factors result in a decrease of the hardness. The lamellar structure is composed of the α2 and the γ phases, which will be softer than the single α2 phase.

3.5. *Discussion of microstructure and mechanical properties*

The homogenization of elemental powders, alloying and plastic deformation during HBM plays an important role in the microstructure evolution during subsequent SPS. Samples P2 and P3 experience significant plastic deformation during HBM and improved homogenization. The speed and duration of HBM influences the kinetic energy experienced by the powders during the milling process.

The changes in the kinetic energy and the possible associated temperature rise results in the improved homogenization in P3 compared to the other powders. The overall milling process and the associated changes in shown schematically in Fig. 10. Fig. 10 (a) shows the morphology of the powder samples (P1-P3) the impact of SPS, and the microstructural changes in P3, subjected to different SPS temperatures. The transition from the granular matrix to a lamellar structure at higher temperatures (1100 °C / 1200 °C) is shown schematically. The impact of microstructural changes in terms of hardness is shown in Fig. 10 (b).

The combined effect of reduced particle size (~2 μm) and the reaction between the powders during SPS leads to differences in the final microstructure between the samples milled at various milling intensities. The average grain size of the α_2-Ti_3Al and γ-TiAl phases of sample S1 is 7 μm and 2.4 μm, respectively. In sample S3 the average grain size of the α_2-Ti_3Al and γ-TiAl phases is 4.5 μm and 1.5 μm respectively. This reduction in grain size of the two phases can lead to a significantly increased hardness of the alloy, following the Hall-Petch relationship. The S3 samples also displayed a significant increase in the volume fraction of α_2-Ti_3Al (~60%), leading to higher hardness of the alloy; α_2-Ti_3Al is harder in comparison to γ-TiAl [17].

In this work, we show that, by combining HBM and SPS of a TiAl alloy, a higher volume fraction of the α_2-Ti_3Al phase and a reduced grain size can be produced, which can enhance certain mechanical properties. Performing SPS at higher temperatures (1100 °C, 1200 °C) leads to the formation of a lamellar structure (Fig. 6(c1) and (d1)) which reduced the hardness compared with the value of 12 GPa observed for the sample (S3) sintered at 1000 °C.

Thus, non-equilibrium processing methods such as SPS, can produce non-lamellar based microstructures with higher hardness than the lamellar structure. There is a HBM speed, duration and SPS process temperature window, in which the desired microstructure can be obtained. Increasing the HBM speed to 500 rpm (not reported in this mss) and the SPS temperature to 1100 °C and 1200 °C did not result in a significant increase in hardness when compared with as cast Ti48Al alloy. Our approach of combining HBM and SPS techniques can produce non-lamellar TiAl alloys with high hardness, at a lower cost and with reduced processing time compared to traditional methods. However, further research is needed to determine the feasibility of scaling up from the laboratory to the industrial level.

4. Conclusions

The microstructure and hardness in Ti-48Al alloy samples prepared by the HBM + SPS processing route was studied.

1. Interestingly, the microstructure of the SPS samples was dominated by the α_2-Ti_3Al phase, without any lamellar structure.
2. A microstructure of equiaxed α_2 and γ grains was observed for a SPS temperature of 1000 °C. At higher temperatures, the lamellar (α_2 + γ) phase transformation occurs in the α phase, resulting in a near lamellar (NL) microstructure.
3. Thus, we conclude that by combining HBM and SPS, high hardness TiAl based alloys with non-lamellar structures can be successfully produced.

Declaration of Competing Interest

The authors declare that they have no known competing financial interests or personal relationships that could have appeared to influence the work reported in this paper.

Data Availability

Data will be made available on request.

Acknowledgments

The authors acknowledge financial support from A*STAR, Singapore under the Structural Metals and Alloys Program (Grant No.: A18B1b0061). The support of the Production Area of Advance (AoA) at Chalmers is acknowledged. ST would like to acknowledge NTU Presidential Postdoctoral Fellowship, Grant number 041NS000761C160.

References

[1] S. Mayer, P. Erdely, F.D. Fischer, D. Holec, M. Kastenhuber, T. Klein, H. Clemens, Intermetallic β-solidifying γ-TiAl based alloys − from fundamental research to application, Adv. Eng. Mater. 19 (2017), 1600735.
[2] B.P. Bewlay, S. Nag, A. Suzuki, M.J. Weimer, TiAl alloys in commercial aircraft engines, Mater. High. Temp. 33 (2016) 549–559.
[3] R.V. Ramanujan, Phase transformations in γ based titanium aluminides, Int. Mater. Rev. 45 (2000) 217–240.
[4] D. Wimler, J. Lindemann, T. Kremmer, H. Clemens, S. Mayer, Microstructure and mechanical properties of novel TiAl alloys tailored via phase and precipitate morphology, Intermetallics 138 (2021), 107316.
[5] K.S. Chan, Y.W. Kim, Influence of microstructure on crack-tip micromechanics and fracture behaviors of a two-phase TiAl alloy, Metall. Trans. A 23 (1992) 1663–1677.
[6] K. Kothari, R. Radhakrishnan, N.M. Wereley, Advances in gamma titanium aluminides and their manufacturing techniques, Prog. Aerosp. Sci. 55 (2012) 1–16.
[7] A. Lasalmonie, Intermetallics: why is it so difficult to introduce them in gas turbine engines? Intermetallics 14 (2006) 1123–1129.
[8] M. Musi, B. Galy, J.-P. Monchoux, A. Couret, H. Clemens, S. Mayer, In-situ observation of the phase evolution during an electromagnetic-assisted sintering experiment of an intermetallic γ-TiAl based alloy, Scr. Mater. 206 (2022), 114233.
[9] N.F. Mogale, W.R. Matizamhuka, Spark plasma sintering of titanium aluminides: a progress review on processing, structure-property relations, alloy development and challenges, Metals 10 (2020) 1080.
[10] Y. Wang, H. Yuan, H. Ding, R. Chen, J. Guo, H. Fu, W. Li, Effects of lamellar orientation on the fracture toughness of TiAl PST crystals, Mater. Sci. Eng. A 752 (2019) 199–205.
[11] Q. Wang, L. Zeng, H. Ding, R. Chen, J. Guo, H. Fu, On the high temperature deformation of a directionally solidified γ-TiAl alloy, Mater. Sci. Eng. A 758 (2019) 19–27.
[12] S.-J. Youn, Y.-K. Kim, S.-W. Kim, K.-A. Lee, Elevated temperature compressive deformation behaviors of γ-TiAl-based Ti–48Al–2Cr–2Nb alloy additively manufactured by electron beam melting, Intermetallics 124 (2020), 106859.
[13] R.V. Ramanujan, P.J. Maziasz, C.T. Liu, The thermal stability of the microstructure of γ-based titanium aluminides, Acta Mater. 44 (1996) 2611–2642.
[14] B. Liu, Y. Liu, Y.P. Li, W. Zhang, A. Chiba, Thermomechanical characterization of β-stabilized Ti–45Al–7Nb–0.4W–0.15B alloy, Intermetallics 19 (2011) 1184–1190.
[15] R.V. Ramanujan, The transformation between the γ and α phases in binary and ternary γ-based titanium aluminides, Acta Metall. Et. Mater. 42 (1994) 2313–2322.
[16] P.J. Maziasz, R.V. Ramanujan, C.T. Liu, J.L. Wright, Effects of B and W alloying additions on the formation and stability of lamellar structures in two-phase γ-TiAl, Intermetallics 5 (1997) 83–95.
[17] J.-P. Monchoux, J. Luo, T. Voisin, A. Couret, Deformation modes and size effect in near-γ TiAl alloys, Mater. Sci. Eng. A 679 (2017) 123–132.
[18] M.A. Morris, T. Lipe, I. Creep deformation of duplex and lamellar TiAl alloys, Intermetallics 5 (1997) 329–337.
[19] O. Guillon, J. Gonzalez-Julian, B. Dargatz, T. Kessel, G. Schierning, J. Ra¨thel, M. Herrmann, Field-assisted sintering technology/spark plasma sintering:

mechanisms, materials, and technology developments, Adv. Eng. Mater. 16 (2014) 830–849.
[20] M. Doubenskaia, A. Domashenkov, I. Smurov, P. Petrovskiy, Study of selective laser melting of intermetallic TiAl powder using integral analysis, Int. J. Mach. Tools Manuf. 129 (2018) 1–14.
[21] Y. Chen, H. Yue, X. Wang, S. Xiao, F. Kong, X. Cheng, H. Peng, Selective electron beam melting of TiAl alloy: microstructure evolution, phase transformation and microhardness, Mater. Charact. 142 (2018) 584–592.
[22] Y. Wang, C. Zhang, Y. Liu, S. Zhao, J. Li, Microstructure characterization and mechanical properties of TiAl-based alloys prepared by mechanical milling and spark plasma sintering, Mater. Charact. 128 (2017) 75–84.
[23] Z. Trzaska, A. Couret, J.-P. Monchoux, Spark plasma sintering mechanisms at the necks between TiAl powder particles, Acta Mater. 118 (2016) 100–108.
[24] T. Voisin, J.-P. Monchoux, L. Durand, N. Karnatak, M. Thomas, A. Couret, An innovative way to produce γ-TiAl Blades: spark plasma sintering, Adv. Eng. Mater. 17 (2015) 1408–1413.
[25] T. Voisin, J.-P. Monchoux, M. Hantcherli, S. Mayer, H. Clemens, A. Couret, Microstructures and mechanical properties of a multi-phase β-solidifying TiAl alloy densified by spark plasma sintering, Acta Mater. 73 (2014) 107–115.
[26] H. Jabbar, J.-P. Monchoux, M. Thomas, F. Pyczak, A. Couret, Improvement of the creep properties of TiAl alloys densified by spark plasma sintering, Intermetallics 46 (2014) 1–3.
[27] T. Voisin, J.-P. Monchoux, M. Perrut, A. Couret, Obtaining of a fine near-lamellar microstructure in TiAl alloys by spark plasma sintering, Intermetallics 71 (2016) 88–97.
[28] Y. Huang, Y. Wang, H. Fan, J. Shen, A. TiAl, based alloy with excellent mechanical performance prepared by gas atomization and spark plasma sintering, Intermetallics 31 (2012) 202–207.
[29] X. Lu, X.B. He, B. Zhang, X.H. Qu, L. Zhang, Z.X. Guo, J.J. Tian, High-temperature oxidation behavior of TiAl-based alloys fabricated by spark plasma sintering, J. Alloy. Compd. 478 (2009) 220–225.
[30] S. Shukla, D.T. Wu, H. Ramanarayan, D. Srolovitz, R.V. Ramanujan, Nanocrystallization in driven amorphous materials, Acta Mater. 61 (2013) 3242–3248.
[31] C. Suryanarayana, Mechanical alloying and milling, Prog. Mater. Sci. 46 (2001) 1–184.
[32] M. Oehring, T. Klassen, R. Bormann, The formation of metastable Ti–Al solid solutions by mechanical alloying and ball milling, J. Mater. Res 8 (1993) 2819–2829.
[33] M. Go¨ken, M. Kempf, W.D. Nix, Hardness and modulus of the lamellar microstructure in PST-TiAl studied by nanoindentations and AFM, Acta Mater. 49 (2001) 903–911.
[34] H. Attar, S. Ehtemam-Haghighi, D. Kent, I.V. Okulov, H. Wendrock, M. Bönisch, A. S. Volegov, M. Calin, J. Eckert, M.S. Dargusch, Nanoindentation and wear properties of Ti and Ti-TiB composite materials produced by selective laser melting, Mater. Sci. Eng.: A 688 (2017) 20–26.
[35] J. Fornell, N. Van Steenberge, A. Varea, E. Rossinyol, E. Pellicer, S. Surin˜ach, M. D. Baro´, J. Sort, Enhanced mechanical properties and in vitro corrosion behavior of amorphous and devitrified Ti40Zr10Cu38Pd12 metallic glass, J. Mech. Behav. Biomed. 4 (2011) 1709–1717.
[36] A. Hynowska, E. Pellicer, J. Fornell, S. Gonz´alez, N. van Steenberge, S. Surin˜ach, A. Gebert, M. Calin, J. Eckert, M.D. Baro´, J. Sort, Nanostructured β-phase Ti–31.0Fe–9.0Sn and sub-μm structured Ti–39.3Nb–13.3Zr–10.7Ta alloys for biomedical applications: microstructure benefits on the mechanical and corrosion performances, Mater. Sci. Eng. C 32 (2012) 2418–2425.
[37] J.C. Schuster, M. Palm, Reassessment of the binary aluminum-titanium phase diagram, J. Phase Equilib. Diffus. 27 (2006) 255–277.
[38] F. Yang, F.T. Kong, Y.Y. Chen, S.L. Xiao, Effect of spark plasma sintering temperature on the microstructure and mechanical properties of a Ti2AlC/TiAl composite, J. Alloy. Compd. 496 (2010) 462–466.